ELSEVIER

Flutter suppression for highly flexible wings using passive and active piezoelectric effects

CrossMark

Natsuki Tsushima, Weihua Su *

Department of Aerospace Engineering and Mechanics, University of Alabama, Box 870280, Tuscaloosa, AL 35487-0280, USA

A B S T R A C T

This paper addresses both active and passive flutter suppressions for highly flexible wings using piezoelectric transduction. An active aeroelastic formulation is used in the studies, featuring a geometrically nonlinear beam formulation coupled with 2-D unsteady aerodynamic equations. The piezoelectric effect is involved in the dynamic nonlinear beam equations, allowing for the aeroelastic studies on multifunctional wings for both piezoelectric energy harvesting and active actuation. In this study, the active piezoelectric actuation is applied as the primary approach for the flutter suppression, with the energy harvesting, as a secondary passive approach, concurrently working to provide an additional damping effect on the wing vibration. The multifunctional system may also convert wing vibration energy to electric energy as an additional function. Moreover, a Linear Quadratic Gaussian controller is developed for the active control of wing limit-cycle oscillations due to the flutter instability. In the numerical studies, both the active and passive flutter suppression approaches are enabled for a highly flexible wing. The impact of the piezoelectric actuator and energy harvester placement on the wing flutter characteristic is explored. This paper presents a comprehensive approach to effectively suppress the aeroelastic instability of highly flexible piezoelectric wings, while allowing to harvest the residual vibration energy. The active multifunctional wing technology that is explored in the paper has the potential to improve the aircraft performance from both aeroelastic stability and energy consumption aspects.

1. Introduction

Recently, for missions of intelligence, surveillance, reconnaissance, environmental researches, etc., highly flexible unmanned airframes have been designed to allow for the high-altitude and long-endurance (HALE) flights. On one hand, the removal of on-board pilots of these aircraft has lifted up a lot of design constraints. On the other hand, HALE flights require very efficient aerodynamic and structural designs, usually resulting in high-aspect-ratio slender wings with a low structural weight fraction. These slender wings may undergo large deformations under normal operation conditions, exhibiting geometrically-nonlinear characters [1,2]. With the highly flexible airframe to achieve the desired high aerodynamic performance in HALE aircraft, a comprehensive understanding and the ability to control the aeroelastic instability resulted from the slenderness of the airframe become particularly important, since such instability may compromise the structural integrity and overall aeroelastic and flight dynamic per-

formance of the complete aircraft. Patil et al. [1–3] used a geometrically nonlinear formulation to characterize the nonlinear behaviors of highly flexible wings and aircraft. They also studied the post-flutter behavior, limit-cycle oscillation (LCO), of a highly flexible wing [2]. Tang and Dowell [4] studied the limit-cycle hysteresis response of a highly flexible wing, still using a nonlinear approach [5] to capture the geometrically nonlinear effects. Dowell et al. [6] also provided a good summary of nonlinear aeroelasticity studies, mainly for flutter and LCO at the time. From these and following studies [3,7–12], it has been well established that aeroelastic design and analysis of highly flexible aircraft should fully take into account their geometrically nonlinear effects. Traditional linear or linearized approaches about the undeformed wing geometry may render erroneous results and conclusions. In recent nonlinear aeroelastic studies, active aeroelastic control of highly flexible wings and aircraft has been a focus of research. From the control perspective, Patil and Hodges [13] designed static output feedback (SOF) controllers for flutter suppression and gust load alleviation of a slender wing using a wing tip flap as its actuator. This SOF controller was also utilized by Dardel and Bakhtiari-Nejad [14] for flutter and LCO controls. Bialy et al. [15] developed an integrated

Nomenclature

$\mathbf{A}$ — Coefficient matrix for state vector in state-space system model

a_0 — Local aerodynamic frame, with a_{0x} axis pointing to wing tip and a_{0y} axis aligned with zero lift line of airfoil

$\mathbf{B}$ — Coefficient matrix for control input in state-space system model

B — Body reference frame

$\bar{\mathbf{B}}$ — Electric displacement .... C/m^2

$\mathbf{B}_{vh}, \mathbf{B}_{va}$ — Piezoelectric coupling matrix for harvester and actuator

$\mathbf{B}^F, \mathbf{B}^M$ — Influence matrices for the distributed forces and moments

B — Semichord of airfoil .... m

$\mathbf{C}$ — Coefficient matrix for state vector in state-space output model

C_p — Capacitance of the energy harvesting system .... F

$\mathbf{D}$ — Coefficient matrix for control input in state-space output model

$\bar{\mathbf{D}}$ — Piezoelectric material stiffness matrix .... Pa

d — Distance of mid-chord in front of reference axis ... m

$\mathbf{E}$ — Electric field .... N/C or V/m

$\mathbf{e}$ — Piezoelectric coupling .... C/m^2

$\mathbf{F}_i$ — Influence matrices in inflow equations with independent variables ($i = 1$, 2, and 3)

$\mathbf{F}^{dist}, \mathbf{F}^{pt}$ — Distributed and point forces

$\mathbf{G}$ — Coefficient matrix for disturbance (process noise) in state-space system model

$\mathbf{g}$ — Gravity acceleration column vector .... m/s^2

$\mathbf{H}$ — Coefficient matrix for disturbance (process noise) in state-space output model

$\mathbf{h}$ — Absolute positions and orientations of beam nodes

J, J_S, J_C — Total system, state, and control cost functions

$\mathbf{J}_{h\varepsilon}, \mathbf{J}_{p\varepsilon}, \mathbf{J}_{\theta\varepsilon}$ — Jacobian matrix

$\mathbf{K}$ — Control filter gain

l_{mc}, m_{mc}, d_{mc} — Aerodynamic lift, moment, and drag on an airfoil about its midchord

$\mathbf{M}_{FF}, \mathbf{C}_{FF}, \mathbf{K}_{FF}$ — Generalized inertia, damping, and stiffness matrices

$\bar{\mathbf{M}}_{FF}, \bar{\mathbf{C}}_{FF}, \bar{\mathbf{K}}_{FF}$ — Linearized generalized inertia, damping, and stiffness matrices

$\mathbf{M}_s, \mathbf{C}_s, \mathbf{K}_s$ — Discrete inertia, damping, and stiffness matrices of whole system

$\mathbf{M}^{dist}, \mathbf{M}^{pt}$ — Distributed and point moments

$\mathbf{N}$ — Influence matrix for the gravity force

$\mathbf{n}$ — Sensor noise

$\mathbf{p}_w$ — Position of w frame resolved in B frame

$\mathbf{Q}, \mathbf{R}$ — Penalty matrix for control input and state vector

Q_e — Total charge accumulated over the electrodes C

r — Weighting term for cost penalty matrix

R_e — Resistance of energy harvesting circuit .... Ω

$\mathbf{R}_F$ — Components of the generalized load vector

$\mathbf{R}_{F/\lambda_0}^{aero}$ — Derivative of the aerodynamic load vector with respect to the inflow states

s — Beam curvilinear coordinate .... m

U_F — Flutter speed .... m/s

U_∞ — Free stream velocity .... m/s

$\mathbf{u}$ — Control input to system plant

v — Voltage of multifunctional system V

$\mathbf{w}$ — Disturbance to system (process noise)

w — Local beam frame resolved in B frame

$\mathbf{x}$ — State vector of system plant

$\hat{\mathbf{x}}$ — State vector estimate of system plant

$\mathbf{y}$ — Output vector of system plant

$\dot{y}, \dot{z}$ — Airfoil translational velocity components resolved in local aerodynamic frame .... m/s

α — Angle of attack .... °

$\dot{\alpha}$ — Airfoil angular velocity about a_{0x} axis .... rad/s

$\boldsymbol{\varepsilon}$ — Total beam strain vector

$\bar{\boldsymbol{\varepsilon}}$ — Material strain in piezoelectric constitutive relation

$\boldsymbol{\varepsilon}_0$ — Initial beam strain vector

ε_x — Extensional strain in beam members

ζ — Permittivity .... F/m or C/V·m

$\boldsymbol{\theta}$ — Rotations of beam nodes .... rad

$\kappa_x, \kappa_y, \kappa_z$ — Twist, flat bending, and edge bending curvature of beam members 1/m

$\boldsymbol{\lambda}$ — Inflow states .... m/s

λ_0 — Inflow velocities .... m/s

ρ — Air density .... kg/m^3

$\bar{\boldsymbol{\sigma}}$ — Material stress in piezoelectric constitutive relation Pa

ω_F — Flutter frequency .... Hz

Subscript

$h\varepsilon$ — $\mathbf{h}$ vector with respect to the strain

$p\varepsilon$ — Nodal position $\mathbf{p}_w$ with respect to the strain $\boldsymbol{\varepsilon}$

$\theta\varepsilon$ — Nodal rotation $\boldsymbol{\theta}$ with respect to the strain $\boldsymbol{\varepsilon}$

eq — Nonlinear equilibrium state

---

sign of error feedback and neural network feedforward controller with a conventional control surface. The controller demonstrated the capability to suppress the LCO and to track the angle of attack, although the control law did not account for actuator limits.

On the other hand, different techniques have been developed and applied to improve the aircraft performance and to facilitate the long-endurance flight, of which wing morphing study has become a dynamic research topic. The morphing aircraft are designed to have the optimum performance over a wide range of flight conditions by actively changing the wing geometry. The morphing wings may also be possible to improve the control authority under poor flight situations. For example, in the studies of the active aeroelastic wing (AAW) [16,17], the morphing technique was implemented to produce the favorable wing aeroelastic deformation so as to improve the aircraft performance. Meanwhile, the multifunctional structural technology [18] is also under development which may also be applied to enhance aircraft performance. This technology integrates two or more structural functions [18,19] and may offer superiority in flight performance. In fact, the applications of active wings and multifunctional structures may be possible to present remarkable improvements in aircraft design.

Obviously, these advanced aerospace structural technologies rely on the advent of active composite materials and structures, such as anisotropic piezo-composite actuators [20,21]. Piezoelectric materials embedded in highly flexible wing structures can be actuated for wing warping and thus for vibration control and/or morphing of the wings. For instance, Bent et al. [22] modeled piezoelectric fiber composites using the Classical Laminated Plate Theory in induced stresses calculations due to anisotropic active materials. Wilkie et al. [23] applied the piezoelectric effects to the aeroelastic analysis of an active twist rotor blade. Cesnik and Ortega-Morales [24] employed a variational method to derive the dynamic equations of an active beam with embedded piezoelectric materials [25].
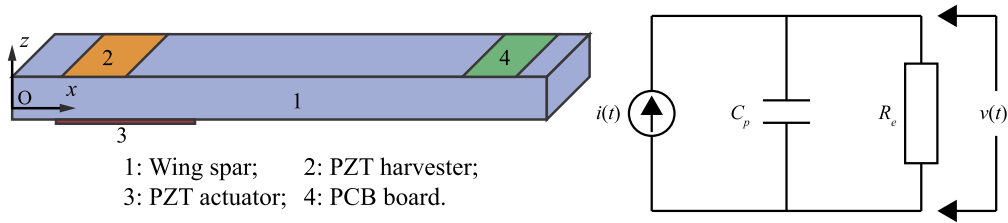
1: Wing spar;   2: PZT harvester;
3: PZT actuator; 4: PCB board.

Fig. 1. Multifunctional beam and equivalent circuit for energy harvesting subsystem.

In addition, one may fully exploit piezoelectric transducers to design multifunctional wings that are capable of both actuation and energy harvesting [26]. In fact, mechanical vibrations of aircraft structural components have been considered as a major consistent energy source [27], with piezoelectric materials embedded into wing structures as sensors and energy harvesters. This is essentially an inversed application of the piezoelectric effect involved in the wing actuation. Various electromechanical models for piezoelectric transducing have been developed to evaluate system performance with piezoelectric transducer. Bilgen et al. [28] developed a piezoelectric cantilever beam model via the linear Euler–Bernoulli beam theory. Wang and Inman [29] used the method for their study of piezoelectric energy harvesting and gust alleviation for a small UAV. Sodano et al. [30] modeled the piezoelectric energy harvesting beam based on the works of Hagood et al. [31] and Crawley and Anderson [32], where the variational method was used to derive electromechanical equations of a piezoelectric beam for energy harvesting. The solution was obtained using the Rayleigh–Ritz method. Subsequently, Anton et al. [19] studied a multifunctional wing for small UAVs.

Based on the achieved knowledge on piezoelectric actuation and energy harvesting in the previous work, the current study aims at actively and concurrently taking advantage of both the functions of piezoelectric transduction in an integral multifunctional wing structure, so as to further improve the aircraft aeroelastic performance. Specifically, the wing flutter instability and its post-flutter behavior (LCO) will be actively controlled by using the piezoelectric actuation in this study. Moreover, the piezoelectric effects of the multifunctional wing will be fully utilized by allowing a concurrent conversion of the wing vibration energy to electric energy, as the shunt damping effects associated to the energy harvesting may passively suppress the wing vibration. Apparently, these multiple functions may interfere or conflict each other during the operation, in that the active control will reduce the wing vibration, which naturally reduces the possible energy output from the harvesters. However, if a certain magnitude of vibration is allowed, provided that it does not harm the wing/aircraft performance, it can serve as a source of the energy harvesting. Therefore, it is of interest to evaluate the tradeoff between the functions and find an optimal balance between them. More importantly, the best tradeoff may change with the instantaneous flight conditions and environment. Therefore, the design should be adaptive to the corresponding condition and allow for a shift of the weight of the functions in the trade-off.

In order to carry out the aeroelastic studies on the multifunctional wings, the piezoelectric actuation and energy harvesting need to be properly modeled in a suitable aeroelastic framework for the highly flexible wings, with the consideration of the aforementioned geometrically nonlinear effects. The traditional approach of modeling the piezoelectric energy harvesting using a linear beam theory are not suitable. In a previous work [33], the authors have modeled the piezoelectric energy harvesting of a highly flexible wing, using a strain-based geometrically nonlinear aeroelastic formulation. The advantages of the strain-based geometrically-nonlinear beam formulation in the studies of highly

flexible structures have been discussed in Su and Cesnik [34]. In a following study [35], concurrent active piezoelectric control and energy harvesting was studied on a highly flexible wing with stochastic gust perturbations. As an advancement to the previous study, this paper will explore both active piezoelectric actuation and energy harvesting (as a passive approach) for the suppression of wing vibrations due to the flutter instability, using the developed strain-based geometrically nonlinear aeroelastic formulation, coupled with the active and passive piezoelectric effects. The value of this study lies in that it combines the piezoelectric active control and shunt damping due to the energy harvesting. It also simultaneously extracts electrical energy from residual vibration, which may further enhance the performance of the aircraft. Such a comprehensive study is not fully explored, although individual studies of piezoelectric active control and energy harvesting from flutter have been previously performed. Therefore, the main goal of this study is to understand how such a multifunctional wing, with a proper control algorithm, may behave beyond the flutter boundary. Specifically, the impact of the piezoelectric actuator and energy harvester placement on the wing flutter performance will be explored in this paper.

2. Theoretical formulation

The theoretical formulation used in the current study is briefly introduced in this section for simplicity purpose, where a slender wing with piezoelectric actuation [35] and energy harvesting [33] is modeled with a strain-based geometrically-nonlinear aeroelastic formulation [8,9,34]. The finite-state inflow theory [36] is incorporated for aerodynamic loads on lifting surfaces. More details of the active aeroelastic formulation can be found in the literature [33,35].

2.1. Multifunctional wing structure

Fig. 1 illustrates a piezoelectric multifunctional beam with both energy harvesting and actuation capabilities. The current work involves modeling of both the piezoelectric energy harvesting [33] and the piezoelectric actuation of such a multifunctional slender structure. For simplicity, the piezoelectric energy harvesting works in the flat bending direction.

The constitutive equation for piezoelectric materials is given as

$$\left\{ \begin{array}{c} \bar{\sigma} \\ \bar{\mathbf{B}} \end{array} \right\} = \left[\begin{array}{cc} \bar{\mathbf{D}} & -\mathbf{e}^T \\ \mathbf{e} & \zeta \end{array} \right] \left\{ \begin{array}{c} \bar{\varepsilon} \\ \mathbf{E} \end{array} \right\} \tag{1}$$

where $\bar{\sigma}$ is the material stress, $\bar{\mathbf{B}}$ is the electric displacement, $\bar{\mathbf{D}}$ is the piezoelectric material stiffness matrix, $\mathbf{e}$ is the piezoelectric coupling, ζ is the permittivity, $\bar{\varepsilon}$ is the material strain, and $\mathbf{E}$ is the electric field, which is obtained from the gradient of the electric voltage v across the piezoelectric layer. The coupled electromechanical effect of piezoelectric material will be considered when deriving the equations of motion.
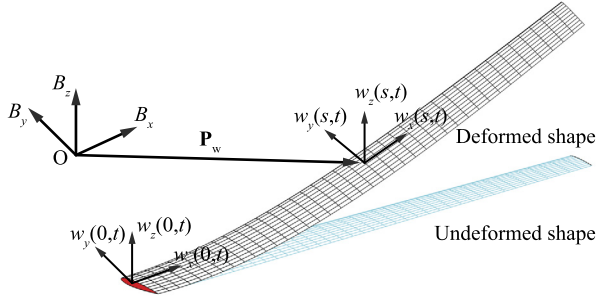
Fig. 2. Beam references frames.

Fig. 3. Airfoil coordinate system and velocity components.

2.2. Equations of motion

A cantilever beam is defined in a fixed frame B. A local beam frame w is built within the B frame as shown in Fig. 2, which defines the position and orientation of each node along the beam reference line. Bases of the beam frame w are $\mathbf{w}_x(s,t)$, $\mathbf{w}_y(s,t)$, and $\mathbf{w}_z(s,t)$, whose directions are pointing along the beam reference axis, toward the leading edge, and normal to the beam surface, respectively, resolved in the B frame. The curvilinear beam coordinate s provides the nodal location in the body frame.

A nonlinear beam element was developed to model the elastic deformation of slender beams in Su and Cesnik [34]. Each of the elements has three nodes and four local strain degrees of freedom, which are extension, twist, flat bending curvature κ_y, and edge bending curvature κ_z of the beam reference line:

$$\boldsymbol{\varepsilon}^T(s) = \left\{ \varepsilon_x(s) \quad \kappa_x(s) \quad \kappa_y(s) \quad \kappa_z(s) \right\} \tag{2}$$

It should not be confused with the strain of the materials ($\bar{\boldsymbol{\varepsilon}}$) in equation (1), although they are related.

The equations of motion can be derived by following the principle of virtual work extended to dynamic system, which is equivalent to Hamilton's Principle. The detailed derivation, where the electromechanical coupling effect was not considered, can be found in Su and Cesnik [8,34]. The electromechanical coupling effect was further discussed and studied for energy harvesting [33]. The complete electro-aeroelastic equations of motion are derived as [33]

$$\mathbf{M}_{FF}\ddot{\boldsymbol{\varepsilon}} + \mathbf{C}_{FF}\dot{\boldsymbol{\varepsilon}} + \mathbf{K}_{FF}\boldsymbol{\varepsilon} = \mathbf{R}_F$$

$$\mathbf{B}_{vh}^T\boldsymbol{\varepsilon} + C_p v + Q_e = 0 \quad \text{or} \quad \mathbf{B}_{vh}^T\dot{\boldsymbol{\varepsilon}} + C_p\dot{v} + \frac{v}{R_e} = 0 \tag{3}$$

where Q_e is the total electric charge accumulated over the electrodes, whose time derivative is the current, C_p is the capacitance of the energy harvester, and R_e is the resistance of the energy harvesting circuit [33]. The generalized inertia, damping, stiffness matrices and generalized force vector are

$$\mathbf{M}_{FF}(\boldsymbol{\varepsilon}) = \mathbf{J}_{h\varepsilon}^T\mathbf{M}_s\mathbf{J}_{h\varepsilon} \qquad \mathbf{C}_{FF}(\boldsymbol{\varepsilon}, \dot{\boldsymbol{\varepsilon}}) = \mathbf{C}_s + \mathbf{J}_{h\varepsilon}^T\mathbf{M}_s\dot{\mathbf{J}}_{h\varepsilon}$$

$$\mathbf{K}_{FF} = \mathbf{K}_s$$

$$\mathbf{R}_F = \mathbf{K}_{FF}\boldsymbol{\varepsilon}_0 + \mathbf{J}_{h\varepsilon}^T\mathbf{Ng} + \mathbf{J}_{p\varepsilon}^T\mathbf{B}^F\mathbf{F}^{dist} + \mathbf{J}_{\theta\varepsilon}^T\mathbf{B}^M\mathbf{M}^{dist} + \mathbf{J}_{p\varepsilon}^T\mathbf{F}^{pt}$$

$$+ \mathbf{J}_{\theta\varepsilon}^T\mathbf{M}^{pt} + \mathbf{B}_v v \tag{4}$$

As shown in equation (4), the generalized force vector involves the effects from initial strains $\boldsymbol{\varepsilon}_0$, gravitational field $\mathbf{g}$, distributed forces $\mathbf{F}^{dist}$, distributed moments $\mathbf{M}^{dist}$, point forces $\mathbf{F}^{pt}$, point moments $\mathbf{M}^{pt}$, and the electric field v. $\mathbf{N}$, $\mathbf{B}^F$, and $\mathbf{B}^M$ are the influence matrices for the gravitational force, distributed forces, and distributed moments, which come from the numerical integration. $\mathbf{B}_v$ is the summation of the electromechanical coupling matrices for both piezoelectric actuators $\mathbf{B}_{va}$ [35] and harvesters $\mathbf{B}_{vh}$ [33].
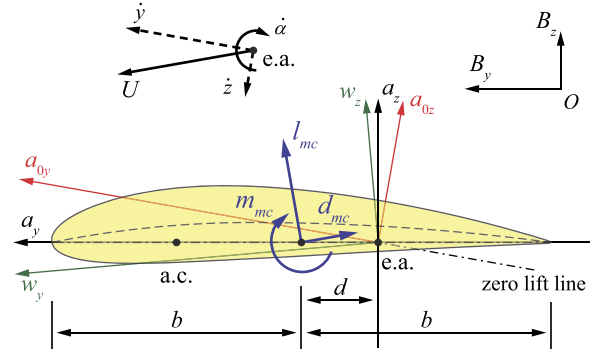
The deformation of the beam reference line is represented by the beam nodal positions and orientations:

$$\mathbf{h}^T(s) = \left\{ \mathbf{p}_w^T(s) \quad \mathbf{w}_x^T(s) \quad \mathbf{w}_y^T(s) \quad \mathbf{w}_z^T(s) \right\}^T \tag{5}$$

where $\mathbf{p}_w$ is the nodal position resolved in the B frame and the orientation is represented by the base vectors of the w frame ($\mathbf{w}_x$, $\mathbf{w}_y$, and $\mathbf{w}_z$). Once the beam strain/curvature is solved from the equations of motion, the deformation of the beam reference line can be recovered from the kinematics [10,34]. The Jacobian matrices shown in equation (4) can also be updated based on the current strain.

2.3. Unsteady aerodynamics

Aerodynamic loads are considered as the distributed loads $\mathbf{F}^{dist}$ and $\mathbf{M}^{dist}$ in equation (4). The unsteady aerodynamic loads used in the current study are based on the two dimensional (2-D) finite-state inflow theory, provided in Peters and Johnson [36]. The theory calculates aerodynamic loads on a thin airfoil section undergoing large motions in an incompressible inviscid subsonic flow. The lift, moment, and drag of a thin 2-D airfoil section about its midchord are given by

$$l_{mc} = \pi\rho b^2(-\ddot{z} + \dot{y}\dot{\alpha} - d\ddot{\alpha})$$

$$+ 2\pi\rho b\dot{y}^2\left[-\frac{\dot{z}}{\dot{y}} + \left(\frac{1}{2}b - d\right)\frac{\dot{\alpha}}{\dot{y}} - \frac{\lambda_0}{\dot{y}}\right]$$

$$m_{mc} = 2\pi\rho b^2\left(-\frac{1}{2}\dot{y}\dot{z} - \frac{1}{2}d\dot{y}\dot{\alpha} - \frac{1}{2}\dot{y}\lambda_0 - \frac{1}{16}b^2\ddot{\alpha}\right)$$

$$d_{mc} = -2\pi\rho b(\dot{z}^2 + d^2\dot{\alpha}^2 + \lambda_0^2 + 2d\dot{\alpha}\dot{z} + 2d\dot{\alpha}\lambda_0) \tag{6}$$

where b is the semichord, and d is the distance of the mid-chord in front of the reference axis. The quantity $-\dot{z}/\dot{y}$ is the angle of attack that consists of the contribution from both the steady state angle of attack and the unsteady plunging motion of the airfoil. The different velocity components are shown in Fig. 3. The inflow velocity λ_0 accounts for induced flow due to free vorticity, which is the weighted summation of the inflow states λ as described Peters and Johnson [36] and governed by

$$\dot{\boldsymbol{\lambda}} = \mathbf{F}_1\ddot{\boldsymbol{\varepsilon}} + \mathbf{F}_2\dot{\boldsymbol{\varepsilon}} + \mathbf{F}_3\boldsymbol{\lambda} \tag{7}$$

The aerodynamic loads about the midchord are transferred to the wing elastic axis and rotated into the fixed B frame for the solution of equations of motion.

2.4. System linearization and flutter analysis

The equation of motion in equation (4) is essentially nonlinear. For both the aeroelastic stability analysis and the control

development of active flutter control, linearization of the nonlinear aeroelastic equations about a nonlinear equilibrium state $\mathbf{x}_{eq}^T = \{\ddot{\boldsymbol{\varepsilon}}_{eq}^T, \dot{\boldsymbol{\varepsilon}}_{eq}^T, \boldsymbol{\varepsilon}_{eq}^T, \boldsymbol{\lambda}_{eq}^T\}$ is performed [35]. Each equation is written with the small perturbation about the nonlinear equilibrium state, which yields the linearized equations as

$$\overline{\mathbf{M}}_{FF}\ddot{\boldsymbol{\varepsilon}} + \overline{\mathbf{C}}_{FF}\dot{\boldsymbol{\varepsilon}} + \overline{\mathbf{K}}_{FF}\boldsymbol{\varepsilon} - \mathbf{R}_{F/\lambda_0}^{aero}\boldsymbol{\lambda} - \mathbf{B}_v\mathbf{v} = \mathbf{0}$$

$$\dot{\boldsymbol{\lambda}} - \mathbf{F}_1\ddot{\boldsymbol{\varepsilon}} - \mathbf{F}_2\dot{\boldsymbol{\varepsilon}} - \mathbf{F}_3\boldsymbol{\lambda} = \mathbf{0} \qquad (8)$$

where $\overline{\mathbf{M}}$, $\overline{\mathbf{C}}$, and $\overline{\mathbf{K}}$ are the linearized general inertia, damping, and stiffness matrices, respectively. $\mathbf{R}_{F/\lambda_0}^{aero}$ is the derivative of the aerodynamic load vector with respect to the inflow states. Equation (8) can be put into the state-space form:

$$\dot{\mathbf{x}} = \mathbf{Ax} + \mathbf{Bu} \qquad (9)$$

where

$$\mathbf{x} = \left\{ \boldsymbol{\varepsilon}^T \quad \dot{\boldsymbol{\varepsilon}}^T \quad \boldsymbol{\lambda}^T \right\}^T \qquad \mathbf{u} = \mathbf{v} \qquad (10)$$

Aeroelastic stability analysis is carried by following the approach in Su and Cesnik [8]. Starting from an initial flow speed, the nonlinear aeroelastic system is linearized and the stability characteristic is evaluated by solving the eigenvalues of the linearized system matrix $\mathbf{A}$ in equation (9). The flutter boundary is found by continuously increasing the flow speed, until the root locus the system crosses the imaginary axis.

2.5. Active control development

A Linear Quadratic Gaussian (LQG) regulator is used in the current study for the active flutter control [35]. The state-space model describing the problem is given as

$$\dot{\mathbf{x}} = \mathbf{Ax} + \mathbf{Bu} + \mathbf{Gw}$$

$$\mathbf{y} = \mathbf{Cx} + \mathbf{Du} + \mathbf{Hw} + \mathbf{n} \qquad (11)$$

where $\mathbf{x}$ is the state vector, $\mathbf{u}$ is the control input to the system plant, $\mathbf{y}$ is a user-defined the system output vector (wing spanwise bending and torsion curvatures in the current study), $\mathbf{w}$ is the disturbance (process noise). Here, local strains are assumed to be measured by a certain sensor (e.g., strain gauges or piezoelectric sensors), with $\mathbf{n}$ being the possible sensor measurement noise. The noises $\mathbf{w}$ and $\mathbf{n}$ are zero-mean white noises. The Kalman filter is to provide an estimated $\hat{\mathbf{x}}$ of to the state $\mathbf{x}$, such that the control input is obtained as

$$\mathbf{u} = -\mathbf{K}\hat{\mathbf{x}} \qquad (12)$$

The performance of the linear quadratic controllers depends on the combination of penalties in the cost function:

$$J = \int_0^\infty (\mathbf{x}^T\mathbf{Qx} + r\mathbf{u}^T\mathbf{Ru})dt \qquad (13)$$

A cost effective controller setting [35] is chosen in this study, where the weighting term r is determined by a trade-off between the state cost and the control cost.

3. Numerical studies

In this section, passive and active flutter suppressions of a highly flexible wing are presented. Particularly, concurrent active piezoelectric actuation and energy harvesting with an LQG controller are explored with different multifunctional wing configurations with variable actuator and energy harvester placement.
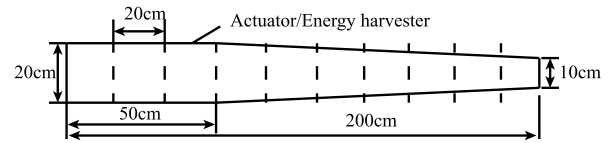
Table 1
Wing geometrical properties.

|	
Airfoil	NACA0014
Span, cm	200
Chord length (at root), cm	20
Taper ratio	1:2
Ref. axis location (from leading edge)	30% of chord
Center of gravity (from leading edge)	30% of chord

Table 2
Material properties for the wing model's cross-section (NACA0014).

	E-Glass	AFC
E1 (GPa)	19.3	42.2
E2 (GPa)	19.3	17.5
E3 (GPa)	9.8	17.5
G12 (GPa)	4.1	5.5
G13 (GPa)	4.1	5.5
G23 (GPa)	3.28	4.4
ν12	0.148	0.354
ν13	0.148	0.354
ν23	0.207	0.496
Thickness (mm)	0.1143	0.127
d11 (pm/V)	–	309
d12 (pm/V)	–	−129
Electrode distance (mm)	–	1.143

Fig. 4. Wing model dimensions.
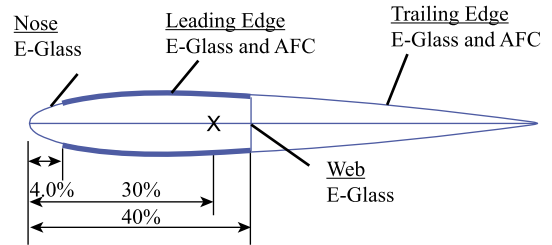
Fig. 5. Lay-ups of the wing cross-section.

3.1. Multifunctional wing

An active wing model [37] is used here for the study of flutter suppression. Since the detailed wing properties can be found in Ref. [37], Tables 1 and 2 only list the basic geometric and material properties of the wing. Fig. 4 shows the wing geometry and Fig. 5 highlights the lay-ups of the wing cross-section. A single passive wing spar is built at 40% chord from the leading edge within the wing cross-section. The wing is divided into ten elements, all with the embedded piezoelectric material to study the passive and active piezoelectric effects on the flutter suppression. The wing elements can all be flexibly "designated" as either active actuators for the vibration control or harvesters for the energy conversion. Although the studies in Ref. [37] covered different actuator orientations from 0° to ±45°, only the actuation oriented at ±22° is performed in the current study to have the balanced bending and torsional actuation capability. Lastly, the piezoelectric resistance load of the energy harvesting circuit is set to be 1 MΩ.

3.2. Stability analysis and flutter boundary

Following the approach introduced in Su and Cesnik [8], a flutter analysis is performed to properly understand the wing's non-

linear aeroelastic stability characteristic. Fig. 6 plots the root loci of the wing where the root angle of attack $\alpha = 8°$ and the free stream velocity U_∞ varies from 60 m/s to 80 m/s at sea level. The gravity is not included in the calculation. The root locus of one mode crosses the imaginary axis at $U_\infty = 71.4$ m/s, which is identified as the flutter boundary. The corresponding flutter mode frequency is $\omega_F = 22.3$ Hz.

The same approach of finding the flutter boundary is used to evaluate the impacts of gravity, altitude (air density), and root angle of attack α on the flutter boundary of the wing. Fig. 7 plots the estimated flutter boundary and the corresponding frequency of the unstable mode at a high altitude of 20,000 m with the change of
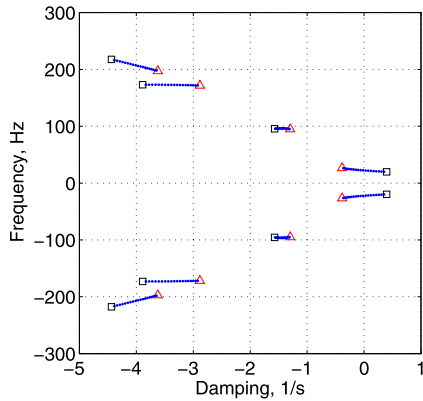
root angle of attack, while Fig. 8 shows the results at sea level. Initially, the flutter speed drops drastically with the increase of α from 0° to 2° (sea level) or 0° to 3° (20,000 m altitude). There is a jump of the flutter speed and frequency around $\alpha = 3.5°$ at the higher altitude. These changes are attributed to the coupling between the edgewise bending and torsion deformations of the wing as discussed in Ref. [3]. The increase of flatwise bending of the wing due to the increase of the root angle of attack (and thus the aerodynamic lift) is in favor of such coupling. Such coupling reduces the effective torsional rigidity of the wing, causing the reduced flutter speed with the increase of the root angle in general. Therefore, the flutter speed also corresponds to the wing tip displacement, which is an indication of the aerodynamic lift (see Fig. 9). The phenomenon of the sudden jump of the flutter speed at the higher altitude was also discussed in Ref. [3], which is due to a shift of wing flutter characteristic with the increase of the wing bending deformation. Such a jump also correlates to the discontinuity of the wing tip deflection plotted in Fig. 9. Even though the flutter speed U_F and frequency ω_F strongly depend on the root angle of attack, the gravity effect seems to be negligible except for the threshold angle where the jump happens (see Fig. 9). Therefore, the gravity force will not be involved in the following analysis for simplicity.

3.3. Time-domain simulation of LCO

The wing flutter analysis is then performed in the time-domain. With the flutter boundary estimated as 71.4 m/s with an 8° root angle of attack at sea level, the instability can be clearly observed when the free stream velocity U_∞ is 74 m/s in a time-domain

Fig. 6. Root loci of the wing at sea level and $\alpha = 8°$ without gravity between $U_\infty = 60$ (triangle) and 80 m/s (square).
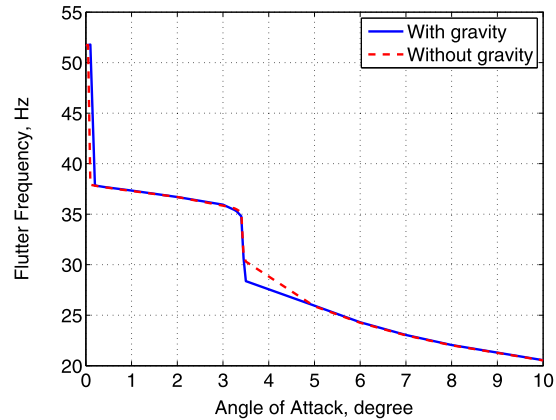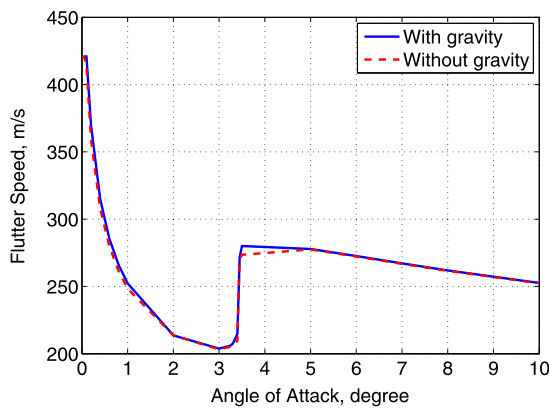

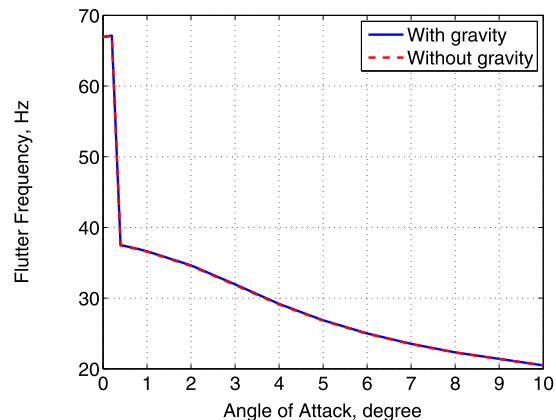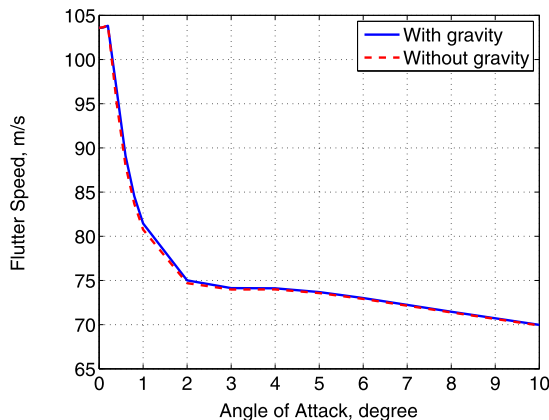Fig. 7. Flutter speed and frequency at 20,000 m altitude.

Fig. 8. Flutter speed and frequency at sea level.

simulation, as shown in Fig. 10. However, the wing vibration dies out if the free stream velocity is only 70 m/s. This time-domain simulation verifies the stability analysis approach and results in the previous section. To gain more aerodynamic damping and for a faster development of the instability, a free stream velocity $U_\infty = 89.25$ m/s (sea level) is then chosen. Fig. 11 shows the wing tip vertical displacements, with the root angles of attack being 5° and 8°, respectively. The phase portraits of wing tip vertical velocity with the wing tip vertical displacement are plotted in Fig. 12. They clearly show the post-flutter behavior of LCO. It is also of

interest to note the different LCOs at different root angles of attack.

3.4. Passive shunt damping with energy harvesting

Energy harvesting has an additional damping effect on the wing vibration [33], which is so-called shunt damping. This damping effect is observed in this section, while a more detailed study of the shunt damping effects on wing vibration was provided in Ref. [35]. To focus on the damping effect due to the energy harvesting, all the elements of the multifunctional wing are activated as harvesters in this study. Fig. 13 shows the wing tip vertical deflections of two aeroelastically neutral cases, while impacted by the energy harvesting subsystem. In the first case, the root angle of attack is $\alpha = 2°$ and the free stream velocity is $U_\infty = 76$ m/s, while the second case has $\alpha = 8°$ and $U_\infty = 73.75$ m/s, both at sea level. Obviously, the shunt damping has a limited impact on the wing behavior and it can only suppress the flutter for few cases ($\alpha = 2°$ for example). This is because the shunt damping is not fully optimized in the current wing design, with the given composite lay-ups.

3.5. Active control of flutter instability

An LQG controller is then developed for active flutter control. Because the LQG estimates the states through the Kalman filter, the filter setting is very important for the feedback control design. In the current study, the Kalman filter is configured based on the flow condition of $U_\infty = 89.25$ m/s. Figs. 14–17 compare the estimated strains using the tuned Kalman filter to the actual strains at the
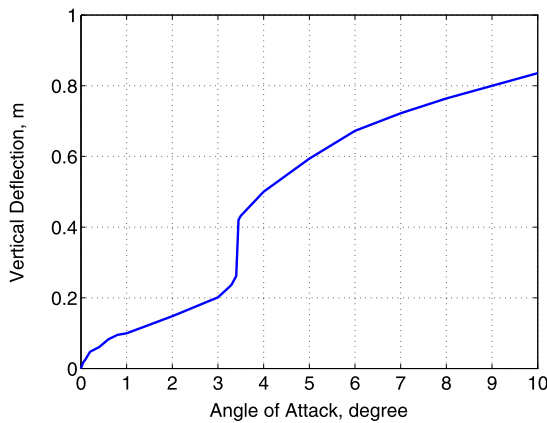

Fig. 9. Static tip displacement with varying root angle of attack and corresponding flow speed of flutter boundary (20,000 m altitude).
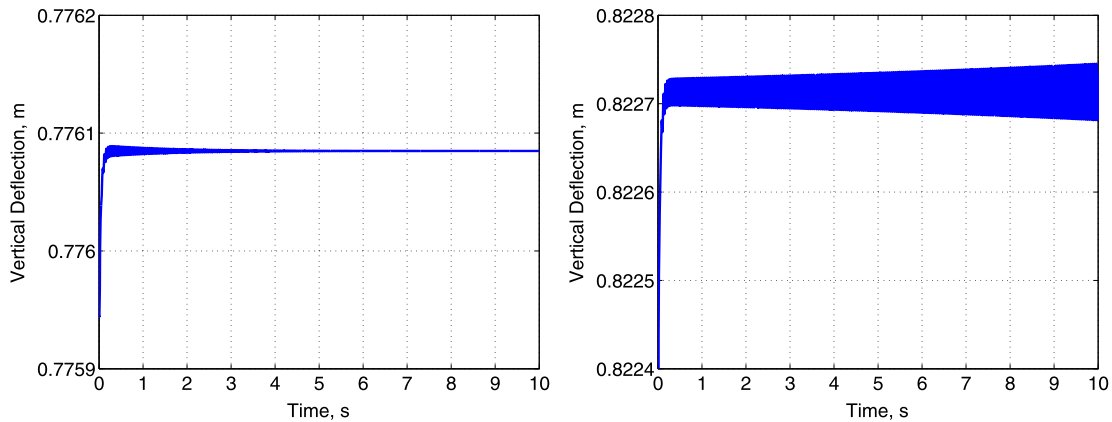

Fig. 10. Wing tip vertical deflection with $\alpha = 8°$ (sea level) at $U_\infty = 71$ m/s (left) and 74 m/s (right).
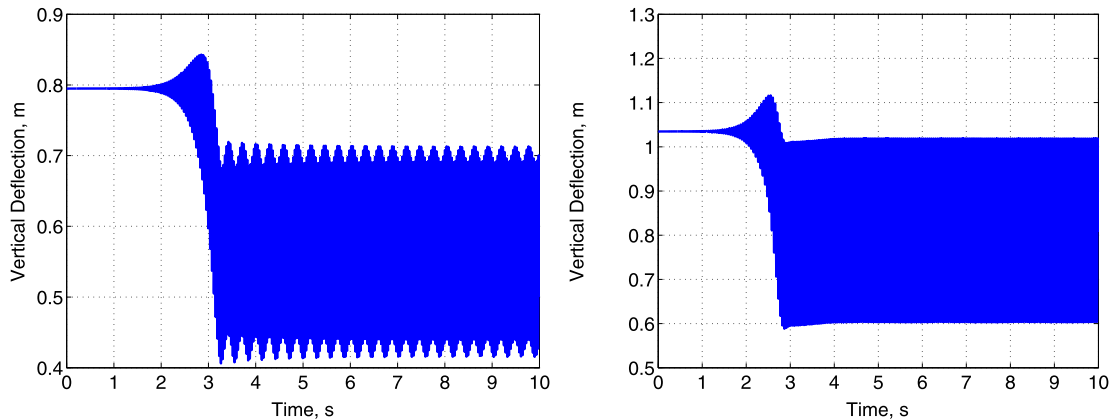

Fig. 11. Wing tip vertical deflection at $U_\infty = 89.25$ m/s (sea level) with $\alpha = 5°$ (left) and 8° (right).
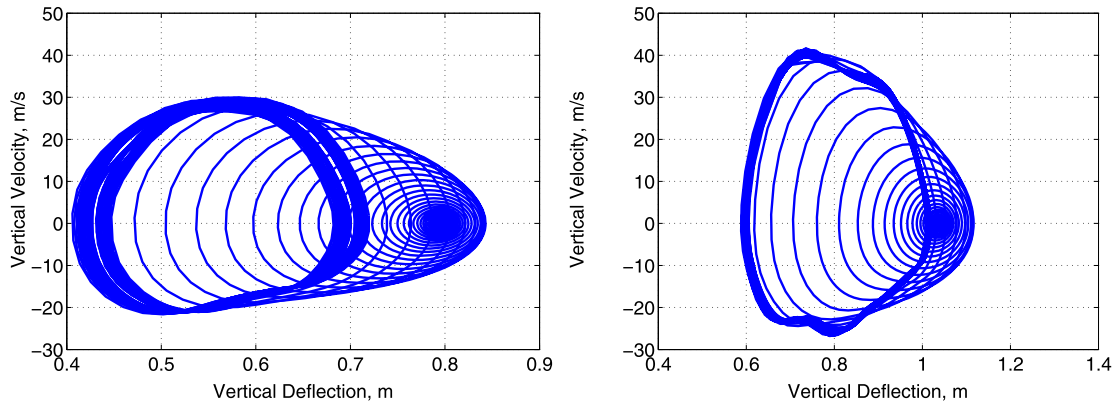
Fig. 12. Wing tip vertical velocity vs. deflection at $U_\infty = 89.25$ m/s (sea level) with $\alpha = 5°$ (left) and $8°$ (right).

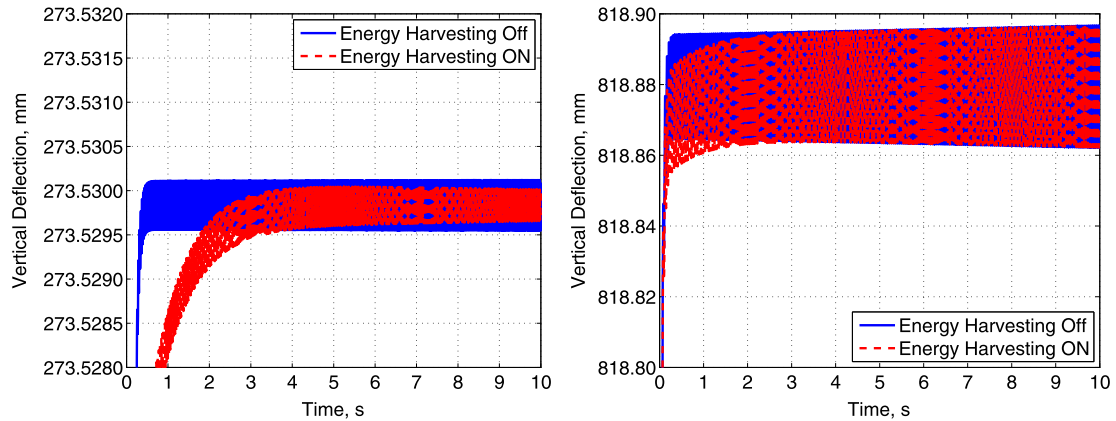**Fig. 13.** Wing tip vertical deflection at $\alpha = 2°$ and $U_\infty = 76$ m/s (left), $\alpha = 8°$ and $U_\infty = 73.75$ m/s (right) with and without energy harvesting.
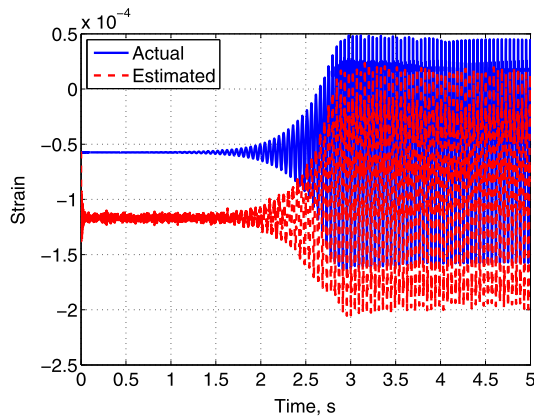

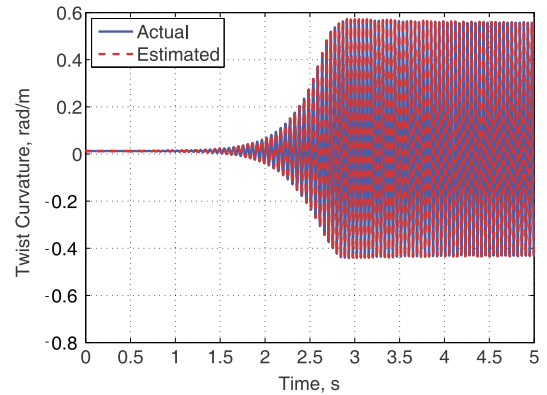**Fig. 14.** Estimated and actual extensional strain.

Fig. 15. Estimated and actual twist curvature.

root of the wing, without using the feedback of control input yet. It is evident that the Kalman filter has been designed to give an accurate estimation of the state.

The controller setting is designed using the approach discussed in Ref. [37], configured accordingly for the flutter suppression in the current study. For the flutter suppression purpose, the wing vibration amplitude should be constrained. Therefore, a stronger vibration state penalty is placed in the controller design by using a higher weighting term $r(1.0 \times 10^{-6})$. Fig. 18 shows the vertical wing tip deflection without and with LQG controller, with full wing span actuated. It can be seen that the LQG stabilizes the wing vibration even when the flow speed is above the flutter boundary.

3.6. Concurrent active and passive flutter suppression

A parametric study of concurrent active flutter control and energy harvesting is presented in this section. Essentially, the study aims at the dual objectives of both flutter suppression and energy harvesting of multifunctional wings. Therefore, both the effectiveness of flutter control and the voltage output from the multifunctional system will be simultaneously explored. The specific focus of the current study is to benchmark different schemes of the actuator/harvester placement and explore their impact on controlling the wing aeroelastic instability. Fig. 19 shows the time-domain snap shots of the LCO. Based on the post-flutter behavior, it can be seen that positions closer to the wing root have higher bending curvatures. Thus, it is more efficient to put controllers closer to the
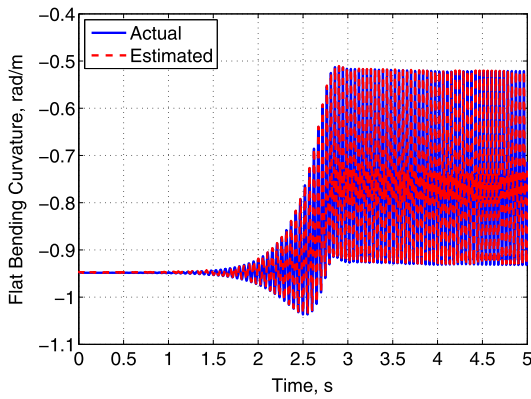
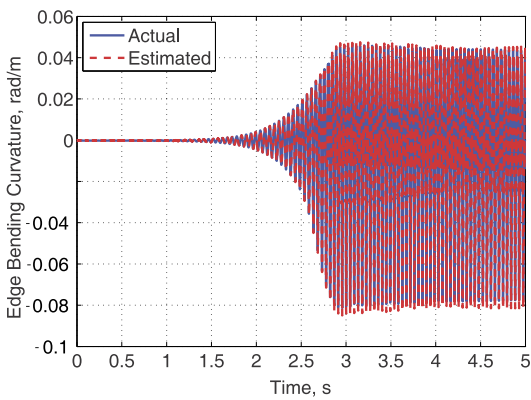**Fig. 16.** Estimated and actual flat bending curvature.

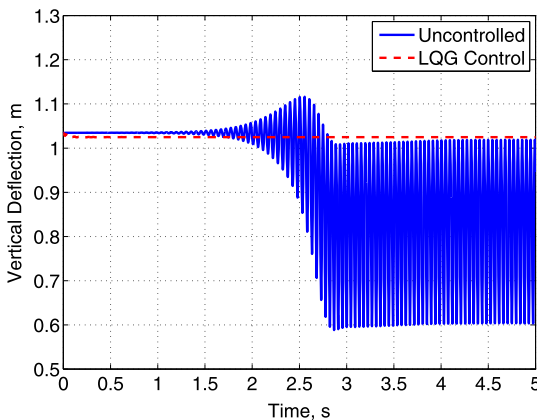**Fig. 17.** Estimated and actual edge bending curvature.

Fig. 18. Wing tip vertical deflection at $U_\infty = 89.25$ m/s and $\alpha = 8°$ without and with LQG (sea level).

wing root for the flutter control purpose. The rest of the elements can be used as energy harvesters to scavenge some vibratory energy.

Starting with the multifunctional configuration in which all the wing element are designated as actuators, various configurations are tested as listed in Table 3. From Configuration 1 to 10, the wing is migrating from a control-dominant configuration to an energy-harvesting dominant one. For example, Configuration 10 has only the root element being activated, allowing the maximum participation of energy harvesters. Note that the wing configurations are such arranged to allow more authority of active wing vibrations control. The operation of the multifunctional wing also allows one to arrange the actuator and harvesters with the priority given to the passive energy harvesting. However, that is not so effective in
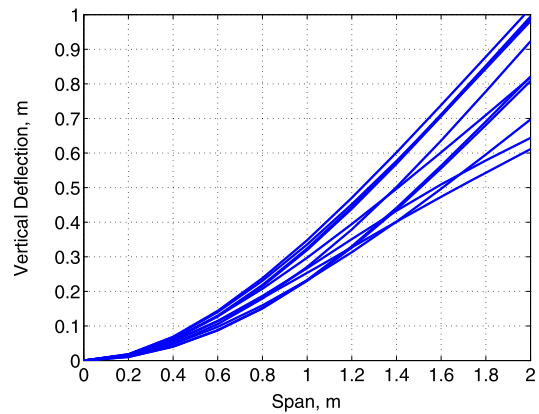

Fig. 19. Snapshots of wing bending deformations at $U_\infty = 89.25$ m/s during limit-cycle oscillation.

terms of the flutter suppression and not included in the current study.

With the same LQG controller designed and applied to the active wing configurations listed in Table 3, the closed-loop simulations with a flow condition ($U_\infty = 89.25$ m/s and $\alpha = 8°$ at sea level) beyond the wing flutter boundary are performed. Fig. 20 shows the wing tip vertical deflection of each multifunctional wing configuration. Configurations 1 to 4 are the most effective options to suppress the flutter vibration. This is intuitive as most of their active materials are actuated for the flutter suppression. The flutter suppression capability is reduced with the reduction of the actuators in Configurations 5 and 6, where LCOs with very small amplitudes (1 cm and 0.5 cm, respectively) can be observed. However, the flutter suppression becomes more effective in Configurations 7 to 9 (compared with Configurations 5 and 6), as one can see the wing vibrations settle back to almost steady deflections. With less elements to be actively controlled in Configurations 7 to 9, their vibration amplitude is reduced compared to Configurations 5 and 6. Therefore, the passive shunt damping effects are playing the role to suppress the vibration. Finally, Configuration 10 cannot provide any flutter control, which shows that the passive shunt-damping is not as effective as the active approach in terms of controlling the flutter vibration. Table 4 lists the root mean square (RMS) output/input voltages from each harvester/actuator in the different configurations. Configurations 1 to 3 have zero or negligible energy output, which agrees with their being control-dominant wing configurations. Configuration 4 is mainly for wing active control. But the wing vibration also allows a certain amount of energy harvesting. Configurations 5 and 9 can harvest a certain amount of energy while controlling the flutter vibration. Their energy outputs are determined by the magnitudes of their residual wing vibrations. The interesting point is that the study shows that the multifunctional wing, designed with a combination of the active control and passive piezoelectric damping, may achieve powerful active control on a few root elements and robust passive shunt damping on the remaining elements. Such an efficient multifunctional wing can also scavenge energy from the residual wing vibration, which would otherwise be wasted without the energy harvesting subsystem. Obviously, the flutter suppression can be further improved for the wing by optimizing the actuator/harvester placement, instead of the sequential placement in this parametric study. For the purpose of evaluating the energy extractions from the harvesters, output currents and powers on the individual elements are further calculated based on the output voltages as presented in Table 5. For example, Configuration 6, which provides the maximum output energy with flutter suppression, can produce the RMS current of 37.106×10^{-3} mA and the RMS power of 28.811×10^{-3} mW with the five harvesters. By assuming this energy can be directly put

Table 3

Multifunctional wing configurations for each simulation case.

Function	Wing configuration									
	1	2	3	4	5	6	7	8	9	10
Actuator element ID	1–10	1–9	1–8	1–7	1–6	1–5	1–4	1–3	1–2	1
Harvester element ID	–	10	9–10	8–10	7–10	6–10	5–10	4–10	3–10	2–10
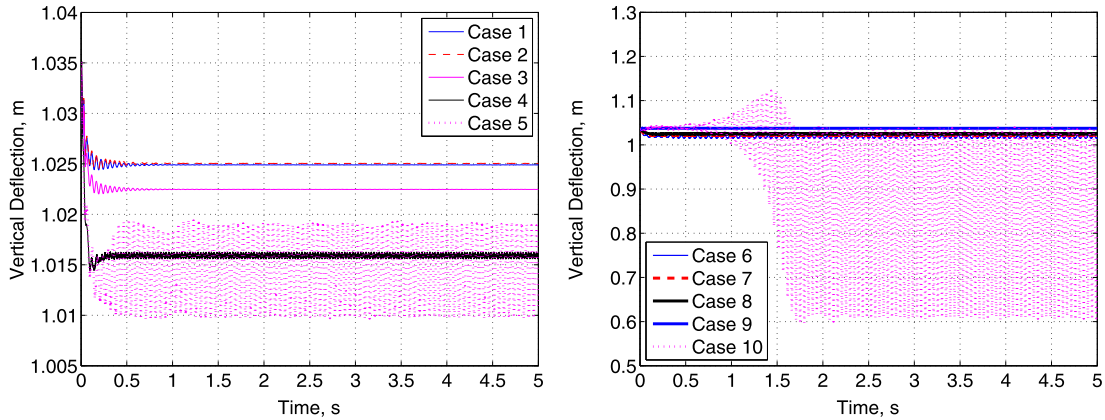
Fig. 20. Wing tip vertical deflection at $U_\infty = 89.25$ m/s with each multifunctional configuration.

Table 4

Root mean square voltage output/input (V_{rms}, V) of each wing configuration.

No.	V_{rms}, V	Element ID (from root)										Total
		1	2	3	4	5	6	7	8	9	10	
1	Output	–	–	–	–	–	–	–	–	–	–	–
	Input	1318.9	480.6	1497.7	1997.9	1998.4	1998.8	1998.9	1849.5	753.2	29.2	13922.9
2	Output	–	–	–	–	–	–	–	–	–	0.204	0.204
	Input	1285.8	446.1	1426.7	1997.7	1998.3	1998.7	1998.8	1828.8	751.2	–	13732.1
3	Output	–	–	–	–	–	–	–	–	0.753	0.222	0.976
	Input	1014.0	856.5	1758.0	1998.0	1998.4	1998.7	1998.8	1774.6	–	–	13397.1
4	Output	–	–	–	–	–	–	–	5.503	5.068	6.597	17.168
	Input	1490.4	1927.2	1999.0	1999.1	1999.1	1999.0	1998.6	–	–	–	13412.3
5	Output	–	–	–	–	–	–	6.226	6.310	5.562	6.132	24.230
	Input	1614.6	1973.1	1999.4	1999.4	1999.4	1999.2	–	–	–	–	11585.1
6	Output	–	–	–	–	–	10.089	5.262	7.141	6.650	7.963	37.106
	Input	1627.2	1953.6	1999.4	1999.4	1999.4	–	–	–	–	–	9579.1
7	Output	–	–	–	–	6.710	5.106	2.324	4.170	4.034	5.265	27.608
	Input	1380.4	1831.0	1999.3	1999.4	–	–	–	–	–	–	7210.1
8	Output	–	–	–	2.998	4.012	2.262	1.409	1.259	1.339	1.907	15.185
	Input	1634.6	1579.8	1866.3	–	–	–	–	–	–	–	5080.7
9	Output	–	–	1.211	0.932	0.811	0.767	0.683	0.555	0.365	0.156	5.479
	Input	1724.3	1180.0	–	–	–	–	–	–	–	–	2904.2
10	Output	–	261.08	186.86	189.16	203.09	209.28	180.09	132.27	83.701	31.251	1476.7
	Input	1999.1	–	–	–	–	–	–	–	–	–	1999.1

Table 5

Root mean square power output (P_{rms}, $\times 10^{-2}$ mW) of each wing configuration.

No.	Element ID (from root)										Total
	1	2	3	4	5	6	7	8	9	10	
2	–	–	–	–	–	–	–	–	–	0.004	0.004
3	–	–	–	–	–	–	–	–	0.057	0.005	0.062
4	–	–	–	–	–	–	–	3.028	2.569	4.352	9.948
5	–	–	–	–	–	–	3.877	3.982	3.093	3.760	14.712
6	–	–	–	–	–	10.179	2.769	5.100	4.422	6.341	28.811
7	–	–	–	–	4.502	2.608	0.540	1.739	1.627	2.772	13.787
8	–	–	–	0.899	1.610	0.512	0.198	0.158	0.179	0.364	3.920
9	–	–	0.147	0.087	0.066	0.059	0.047	0.031	0.013	0.002	0.451
10	–	6816.0	3491.6	3578.1	4124.4	4379.6	3242.7	1749.4	700.58	97.661	28180.0

into an external storage without an energy loss, the energy amount of 1.04 Wh from the five harvesters is more than the energy capacity of 0.9 Wh provided by a common rechargeable battery (e.g., Energizer Recharge® rechargeable batteries). As the batteries are used for a lot of electronics operations, the harvested energy can be used for onboard electronics operations or directly recycled to support the wing actuation.

4. Conclusion

An approach for studying the flutter suppression using both active and passive piezoelectric effects was discussed in the paper. The piezoelectric effects were modeled in a strain-based geometrically nonlinear aeroelastic formulation. The coupled electro-aeroelastic model enables the prediction of the transient electric outputs and the mechanical deformations of the electro-aeroelastic system. The nonlinear electro-aeroelastic formulation is suitable for both the active piezoelectric actuation and energy harvesting studies for highly flexible wings. Based on the formulation, an LQG controller was applied to regulate piezoelectric actuation.

A multifunctional wing having bending/torsional actuation capability was considered for active control and energy harvesting with the flutter instability. Flutter characteristics of the wing were investigated by evaluating the root locus of the linearized aeroelastic system. Time-domain simulations verified the frequency-domain stability analysis results and also provided actual temporal wing behavior. The shunt damping effects from energy harvesting function on the flutter was then investigated. The energy harvesting could provide an additional passive damping effect and was helpful to stabilize the wing in some cases, yet not being very efficient in flutter suppression for every case. That is why an LQG controller was also used for the active flutter control. It was designed by setting to have the cost-effective control of vibration, allowing for the active flutter suppression.

Finally, the concurrent active piezoelectric actuation control of flutter and energy harvesting were studied for the multifunctional wing. Several device placements of the multifunctional wing were tested to parametrically study the performance of the multifunctional system, especially the flutter suppression. Most of the dual-functional wings may provide their flutter suppression capability, while the one with only the root element as an actuator was completely ineffective in suppressing the flutter. The interesting point was that for efficient flutter suppression, the multifunctional wing could be designed with a combination of the active control and passive piezoelectric damping. It also successively scavenged energy from the residual wing vibration, which would otherwise be wasted without the energy harvesting subsystem.

In conclusion, this study demonstrated the effectiveness of the flutter suppression concurrently using the active and passive effects of the piezoelectric materials embedded in a highly flexible wing. By properly place the piezoelectric actuators and energy harvesters, it was possible to stabilize the wing, while extracting a certain amount energy, both of which would contribute to improving the performance of the wing and aircraft. It is important to note that the amount of energy that can be harvested is dependent on the amplitude of the residual vibration after the active control of the wing. Therefore, the optimum performance of such active control and energy harvesting system is subject to further optimization of the layups of the active materials and the control scheme.

Conflict of interest statement

There is no conflict of interest.

References

[1] M.J. Patil, D.H. Hodges, C.E.S. Cesnik, Nonlinear aeroelastic analysis of complete aircraft in subsonic flow, J. Aircr. 37 (2000) 753–760.

[2] M.J. Patil, D.H. Hodges, C.E.S. Cesnik, Limit-cycle oscillations in high-aspect-ratio wings, J. Fluids Struct. 15 (2001) 107–132.

[3] M.J. Patil, D.H. Hodges, C.E.S. Cesnik, Nonlinear aeroelasticity and flight dynamics of high-altitude long-endurance aircraft, J. Aircr. 38 (2001) 88–94.

[4] D.M. Tang, E.H. Dowell, Limit-cycle hysteresis response for a high-aspect-ratio wing model, J. Aircr. 39 (2002) 885–888.

[5] D. Tang, E.H. Dowell, Experimental and theoretical study on aeroelastic response of high-aspect-ratio wings, AIAA J. 39 (2001) 1430–1441.

[6] E. Dowell, J. Edwards, T. Strganac, Nonlinear aeroelasticity, J. Aircr. 40 (2003) 857–874.

[7] C.M. Shearer, C.E.S. Cesnik, Nonlinear flight dynamics of very flexible aircraft, J. Aircr. 44 (2007) 1528–1545.

[8] W. Su, C.E.S. Cesnik, Nonlinear aeroelasticity of a very flexible blended-wing-body aircraft, J. Aircr. 47 (2010) 1539–1553.

[9] W. Su, C.E.S. Cesnik, Dynamic response of highly flexible flying wings, AIAA J. 49 (2011) 324–339.

[10] C.E.S. Cesnik, E.L. Brown, Modeling of High Aspect Ratio Active Flexible Wings for Roll Control, in: 43rd AIAA/ASME/ASCE/AHS Structures, Structural Dynamics, and Materials Conferences, AIAA, Denver, CO, 2002.

[11] C.E.S. Cesnik, W. Su, Nonlinear aeroelastic modeling and analysis of fully flexible aircraft, in: 46th AIAA/ASME/ASCE/AHS/ASC Structures, Structural Dynamics, and Materials Conference, AIAA, Austin, TX, 2005.

[12] C.-S. Chang, D.H. Hodges, M.J. Patil, Flight dynamics of highly flexible aircraft, J. Aircr. 45 (2008) 538–545.

[13] M.J. Patil, D.H. Hodges, Output feedback control of the nonlinear aeroelastic response of a slender wing, J. Guid. Control Dyn. 25 (2002) 302–308.

[14] M. Dardel, F. Bakhtiari-Nejad, Limit cycle oscillation control of wing with static output feedback control method, Aerosp. Sci. Technol. 24 (2013) 147–160.

[15] B.J. Bialy, C.L. Pasiliao, H.T. Dinh, W.E. Dixon, Tracking control of limit cycle oscillations in an aero-elastic system, J. Dyn. Syst. Meas. Control 136 (2014) 1–5.

[16] E. Pendleton, P. Flick, D. Paul, D.F. Voracek, E. Reichenbach, K. Griffin, The X-53 a summary of the active aeroelastic wing flight research program, in: 48th AIAA/ASME/ASCE/AHS/ ASC Structures, Structural Dynamics and Materials Conference and Exhibit, AIAA, Honolulu, Hawaii, 2007.

[17] D.F. Voracek, E. Pendleton, E. Reichenbach, K. Griffin, L. Welch, The Active Aeroelastic Wing Phase I Flight Research through January 2003, National Aeronautics and Space Administration, Dryden Flight Research Center, 2004.

[18] L. Christodoulou, J.D. Venables, Multifunctional material systems: the first generation, J. Miner. Met. Mater. Soc. 55 (2003) 39–45.

[19] S.R. Anton, A. Erturk, D.J. Inman, Multifunctional unmanned aerial vehicle wing spar for low-power generation and storage, J. Aircr. 49 (2012) 292–301.

[20] A.A. Bent, Active fiber composite material systems for structural control applications, in: H.J. Jack (Ed.), Smart Structures and Materials 1999: Industrial and Commercial Applications of Smart Structures Technologies, SPIE, Newport Beach, CA, 1999, pp. 166–177.

[21] R.B. Williams, G. Park, D.J. Inman, W.K. Wilkie, An overview of composite actuators with piezoceramic fibers, in: 20th International Modal Analysis Conference, Los Angeles, CA, 2002, pp. 421–427.

[22] A.A. Bent, N.W. Hagood, J.P. Rodgers, Anisotropic actuation with piezoelectric fiber composites, J. Intell. Mater. Syst. Struct. 6 (1995) 338–349.

[23] W.K. Wilkie, W.K. Belvin, K.C. Park, Aeroelastic analysis of helicopter rotor blades incorporating anisotropic piezoelectric twist actuation, in: World Congress and Exposition, 1996, pp. 423–434.

[24] C.E.S. Cesnik, M. Ortega-Morales, Active beam cross-sectional modeling, J. Intell. Mater. Syst. Struct. 12 (2001) 483–496.

[25] C.E.S. Cesnik, S. Shin, Structural Analysis for Designing Rotor Blades with Integral Actuators, in: 39th Structures, Structural Dynamics, and Materials Conference, AIAA, Long Beach, CA, 1998.

[26] A. Erturk, D.J. Inman, Piezoelectric Energy Harvesting, John Wiley & Sons, Hoboken, NJ, 2011, pp. 1–94, pp. 151–385.

[27] C. De Marqui Jr, A. Erturk, D.J. Inman, An electromechanical finite element model for piezoelectric energy harvester plates, J. Sound Vib. 327 (2009) 9–25.

[28] O. Bilgen, Y. Wang, D.J. Inman, Electromechanical comparison of cantilevered beams with multifunctional piezoceramic devices, Mech. Syst. Signal Process. 27 (2012) 763–777.

[29] Y. Wang, D.J. Inman, Simultaneous energy harvesting and gust alleviation for a multifunctional composite wing spar using reduced energy control via piezoceramics, J. Compos. Mater. 47 (2013) 125–146.

[30] H.A. Sodano, G. Park, D.J. Inman, Estimation of electric charge output for piezoelectric energy harvesting, Strain 40 (2004) 49–58.

[31] N.W. Hagood, W.H. Chung, A. von Flotow, Modelling of piezoelectric actuator dynamics for active structural control, J. Intell. Mater. Syst. Struct. 1 (1990) 327–354.

[32] E.F. Crawley, E.H. Anderson, Detailed models of piezoceramic actuation of beams, J. Intell. Mater. Syst. Struct. 1 (1990) 4–25.

[33] N. Tsushima, W. Su, Modeling of highly flexible multifunctional wings for energy harvesting, J. Aircr. 53 (2016) 1033–1044.

[34] W. Su, C.E.S. Cesnik, Strain-based geometrically nonlinear beam formulation for modeling very flexible aircraft, Int. J. Solids Struct. 48 (2011) 2349–2360.

[35] N. Tsushima, W. Su, Concurrent active piezoelectric control and energy harvesting of highly flexible multifunctional wings, J. Aircr. (2016), http://dx.doi.org/10.2514/1.C033846, published online 3 October 2016.

[36] D.A. Peters, M.J. Johnson, Finite-state airloads for deformable airfoils on fixed and rotating wings, in: Symposium on Aeroelasticity and Fluid Structure Interaction Problems, ASME Winter Annual Meeting, The American Society of Mechanical Engineering, New York, NY, 1994, pp. 1–28.

[37] M. Ortega-Morales, Modeling and Control of the Aeroelastic Response of Highly Flexible Active Wings, Massachusetts Institute of Technology, Cambridge, MA, 2000.